Received: 28 August 2019 | Revised: 27 December 2019 | Accepted: 19 January 2020

DOI: 10.1002/mrm.28208

FULL PAPER

Magnetic Resonance in Medicine

Time-domain principal component reconstruction (tPCR): A more efficient and stable iterative reconstruction framework for non-Cartesian functional MRI

Fei Wang[1,2] | **Jürgen Hennig**[1,2] | **Pierre LeVan**[1,3,4]

[1]Department of Radiology, Medical Physics, Faculty of Medicine, Medical Center - University of Freiburg, Freiburg, Germany

[2]Center for Basics in NeuroModulation (NeuroModul Basics), Faculty of Medicine, University of Freiburg, Freiburg, Germany

[3]Departments of Radiology and Paediatrics, Cumming School of Medicine, University of Calgary, Calgary, Canada

[4]Alberta Children's Hospital Research Institute and Hotchkiss Brain Institute, University of Calgary, Calgary, Canada

Correspondence
Fei Wang, Department of Radiology, Medical Physics, Medical Center - University of Freiburg, Faculty of Medicine, University of Freiburg, Freiburg, Germany.
Email: fei.wang@uniklinik-freiburg.de

Funding information
China Scholarship Council; Deutsche Forschungsgemeinschaft, Grant/Award Number: EXC-1086 and He 1875/28-1

Purpose: To improve the reconstruction efficiency (i.e., computational load) and stability of iterative reconstruction for non-Cartesian fMRI when using high undersampling rates and/or in the presence of strong off-resonance effects.

Theory and Methods: The magnetic resonance encephalography (MREG) sequence with 3D non-Cartesian trajectory and 0.1s repetition time (TR) was applied to acquire fMRI datasets. Different from a conventional time-point-by-time-point sequential reconstruction (SR), the proposed time-domain principal component reconstruction (tPCR) performs three steps: (1) decomposing the k-t-space fMRI datasets into time-domain principal component space using singular value decomposition, (2) reconstructing each principal component with redistributed computation power according to their weights, and (3) combining the reconstructed principal components back to image-t-space. The comparison of reconstruction accuracy was performed by simulation experiments and then verified in real fMRI data.

Results: The simulation experiments showed that the proposed tPCR was able to significantly reduce reconstruction errors, and subsequent functional activation errors, relative to SR at identical computational cost. Alternatively, at fixed reconstruction accuracy, computation time was greatly reduced. The improved performance was particularly obvious for L1-norm nonlinear reconstructions relative to L2-norm linear reconstructions and robust to different regularization strength, undersampling rates, and off-resonance effects intensity. By examining activation maps, tPCR was also found to give similar improvements in real fMRI experiments.

Conclusion: The proposed proof-of-concept tPCR framework could improve (1) the reconstruction efficiency of iterative reconstruction, and (2) the reconstruction stability especially for nonlinear reconstructions. As a practical consideration, the

improved reconstruction speed promotes the application of highly undersampled non-Cartesian fast fMRI.

KEYWORDS

convergence speed, fast fMRI, iterative reconstruction, PCA/SVD, stability

1 | INTRODUCTION

FMRI detects brain activity by measuring BOLD signals.[1] Even though the BOLD signals change slowly and smoothly, which makes standard 2D EPI sampling with a 2-3 seconds temporal resolution generally sufficient,[2] rapid sampling is still highly beneficial for the following purposes: (1) detection of high-frequency BOLD oscillations (up to nearly 1Hz) reflecting potentially relevant brain activity[3,4]; (2) better characterization of the hemodynamic response function (HRF), which is subtly different across subjects and cortical areas[5-7]; (3) separation of physiological noise, such as breathing and cardiac pulsation[8-12]; and (4) greater statistical power and sensitivity.[13-16] Thus, rapid fMRI techniques are of great practical significance and can markedly improve fMRI analyses.[17,18]

Reducing the acquisition duration of individual images usually involves combinations of parallel imaging,[19-21] k-space undersampling[22] and/or optimized non-Cartesian sampling patterns.[23-27] With these complex sampling strategies, image reconstruction becomes challenging. In particular, the reconstruction quality is dominated by the rate of k-space undersampling, which may result in ill conditioning of the inverse problem. Moreover, if readout duration is long, off-resonance effects also become an important interference factor that also contributes to ill conditioning and can only be partially corrected.[28-30]

In fMRI, the images are usually reconstructed time-point-by-time-point. Especially with ultra-fast imaging techniques necessitating highly undersampled acquisitions and iterative reconstruction algorithms, high computational requirements may become an issue and some reconstruction errors are inevitable. The time-point-by-time-point reconstruction fails to take advantage of the high redundancy between successive fMRI images, which could be used to alleviate the computational load of the reconstruction. Moreover, any reconstruction error may negate the potential gains in sensitivity from increasing the temporal resolution of fMRI, as even small errors relative to the MR signal may still be significant relative to temporal BOLD signal changes, leading to spurious fluctuations and reduced temporal signal-to-noise-ratio (tSNR).

Instead, separation reconstruction is a spatiotemporal integrated reconstruction strategy, which decomposes the k-t-space data into background and dynamic components. The background could be defined as the temporal average of k-t-space data,[31-33] or a low-rank (rather than static) background.[34-36] The dynamic components are then the difference from the background. If the dynamic components are sparse, they could potentially be reconstructed better. The separation method has been shown to perform well in applications such as dynamic contrast-enhanced MRI (DCE-MRI), where the boundary between background and sparse component is clear. However, in fMRI, it may be more difficult to separate the background and sparse components. For example, in resting-state fMRI, the signals of interest are actually background fluctuations that might not necessarily be sparse.

The partial separation model is another spatiotemporal integrated reconstruction strategy.[37-43] It supposes that the spatiotemporal signals could be well represented by a low-rank model based on principal component analysis (PCA). This could involve different sampling patterns at each time frame followed by interpolation of the missing k-t-space data using low-rank constraints. However, in fMRI studies, especially those focusing on high-frequency fluctuations, it is not clear to which extent high-rank information contributes to brain activity signals. Moreover, the time-varying sampling patterns may potentially introduce time-varying noise, for example due to variable off-resonance behaviors, which are difficult to correct.

This paper proposes a generalized spatiotemporal integrated framework to improve the iterative reconstruction of ultra-fast fMRI, particularly in the presence of strong off-resonance effects.[44] It is based on non-time-varying sampling strategies (without assuming sparsity in the temporal dimension). This study focuses on the magnetic resonance encephalography (MREG) technique, which combines parallel sampling, a high undersampling rate and an optimized 3D non-Cartesian trajectory to realize full brain data acquisition in a single excitation.[23-25] The high temporal resolution leads to a large number of images to reconstruct (typically in the thousands). Combining this with the need for 3D iterative reconstruction requiring dozens of central processing unit (CPU)-minutes for each image, the computational load to reconstruct an entire fMRI dataset may easily become impractical. The dynamic image reconstruction framework is described in detail and evaluated in simulations as well as experimentally using breath-hold experiments. The applicability to other iterative algorithms is then discussed.

2 | THEORY

2.1 | Regularized iterative SENSE reconstruction

The MR image reconstruction requires solving the following equation:

$$\boldsymbol{s} = \mathbf{F}\boldsymbol{\rho} + \epsilon, \tag{1}$$

where $\boldsymbol{s}$ is the acquired k-space data; $\boldsymbol{\rho}$ is the unknown image; $\mathbf{F}$ is the forward operator encoding coil sensitivities, k-space trajectory, and off-resonance effects; and ϵ is noise. We consider the case where $\boldsymbol{\rho}$ cannot be reconstructed by inverting $\mathbf{F}$ directly because it is too large and does not have a tractable analytical solution. In this case, reconstruction is commonly performed by iterative algorithms.[26] The forward operator may be ill conditioned due to undersampling or off-resonance effects, whereas regularization can be used to improve the conditioning by constraining certain image properties.

The image reconstruction is defined as searching for the minimum of a cost function $c(\boldsymbol{\rho})$ incorporating a data fidelity term and a regularization term such as an L2-norm penalty:

$$c(\hat{\boldsymbol{\rho}}) = \|\mathbf{F}\hat{\boldsymbol{\rho}} - \boldsymbol{s}\|_2^2 + \lambda^2 \|\mathbf{R}\hat{\boldsymbol{\rho}}\|_2^2, \tag{2}$$

here, $\|\cdot\|_2^2$ indicates squared L2-norm, $\mathbf{R}$ is some image transform, and λ is a regularization parameter. As long as the forward operator $\mathbf{F}$ and the transform $\mathbf{R}$ are linear operators, the cost function can be minimized by an algorithm such as linear conjugate gradient (CG). It admits a closed-form solution $\hat{\boldsymbol{\rho}} = \left(\mathbf{F}^{\mathrm{T}}\mathbf{F} + \lambda^2\mathbf{R}\right)^{-1}\mathbf{F}^{\mathrm{T}}\boldsymbol{s} = \mathrm{f}_{\mathrm{l2}}(\boldsymbol{s})$, where the inverse operator f_{l2} is data independent.

In order to exploit sparse image properties, there is also great interest in using regularization based on the L1-norm:

$$c(\hat{\boldsymbol{\rho}}) = \|\mathbf{F}\hat{\boldsymbol{\rho}} - \boldsymbol{s}\|_2^2 + \lambda \|\mathbf{R}\hat{\boldsymbol{\rho}}\|_1, \tag{3}$$

here, $\|\cdot\|_1$ indicates L1-norm. Note that minimizing this cost function requires a nonlinear iterative algorithm and cannot be represented as a closed-form solution. Let $\hat{\rho} = \mathrm{f}_{\mathrm{l1}}(\mathrm{s})$, then the inverse operator f_{l1} is data dependent.

As the data fidelity and regularization terms no longer have the same scaling – unlike with L2-regularization, where both terms scale according to $\|\hat{\boldsymbol{\rho}}\|_2^2$ – it should also be noted that the parameter λ will depend on image scaling. For example, for a dataset with a different magnitude than a given reference dataset, the regularization parameter has to be scaled relative to the reference in order to obtain the same degree of regularization:

$$\lambda = \frac{\|\boldsymbol{s}\|_2}{\|\boldsymbol{s}_{\mathrm{ref}}\|_2}\lambda_{\mathrm{ref}}. \tag{4}$$

2.2 | Time-domain principal component reconstruction (tPCR)

For fMRI, an additional time dimension is introduced. The conventional time-point-by-time-point reconstruction is referred to as sequential reconstruction (SR). This paper proposes a principal component-based reconstruction framework, time-domain principal component reconstruction (tPCR), which transforms the reconstruction domain from spatiotemporal space to principal component space.

Before reconstruction, a PCA or singular value decomposition (SVD) is performed along the time dimension

$$\boldsymbol{s}(\boldsymbol{k}, t) = \sum_{l=1}^{T} \boldsymbol{u}_l(\boldsymbol{k})\,\varepsilon_l \boldsymbol{v}_l(t) = \sum_{l=1}^{T} \boldsymbol{U}_l(\boldsymbol{k})\,\boldsymbol{v}_l(t), \tag{5}$$

in which $\{\boldsymbol{u}_l(\boldsymbol{k})\}$ and $\{\boldsymbol{v}_l(t)\}$ are left and right singular vectors representing the spatial and temporal parts of the principal components. $\{\varepsilon_l\}$, the singular values arranged in decreasing order, are the weighting function of each component. Combining $\{\boldsymbol{u}_l(\boldsymbol{k})\}$ and $\{\varepsilon_l\}$ to $\{\boldsymbol{U}_l(\boldsymbol{k})\}$ constructs a weighted spatial part. The $\{\boldsymbol{U}_l(\boldsymbol{k})\}$ is then reconstructed from k-space to image-space component-by-component $\{\boldsymbol{P}_l(\boldsymbol{r})\}$. Finally, they are recombined with the temporal part by a cross product to image-t-space.

$$\boldsymbol{I}(\boldsymbol{r}, t) = \sum_{l=1}^{T} \mathrm{f}_{\mathrm{l2/l1}}\left(\boldsymbol{U}_l(\boldsymbol{k})\right)\boldsymbol{v}_l(t) = \sum_{l=1}^{T} \boldsymbol{P}_l(\boldsymbol{r})\,\boldsymbol{v}_l(t) \tag{6}$$

The flowcharts of SR and tPCR are compared in Figure 1.

2.3 | Redistributed computational power

In contrast to SR where the signal at each time point has the same weight, the weights of the principal components are redistributed by ever-decreasing $\{\varepsilon_l\}$, which allows redistributing the number of CG iterations among the components according to their weights; components with low weights can be reconstructed using fewer iterations since they contribute less to the total signal, and vice versa. Specifically, if the first principal component corresponding to eigenvalue ε_1 is reconstructed within a given tolerance (relative reconstruction error) *tol*, then the l^{th} component will need to be reconstructed only within a tolerance $tol \times (\varepsilon_1/\varepsilon_l)$ in order to contribute the same reconstruction error in the recombined signal. In CG, the required number of iterations grows asymptotically with the logarithm of the target tolerance[45]:

$$n = \frac{1}{2}\sqrt{\kappa}\ln\left(\frac{2}{tol}\right), \tag{7}$$

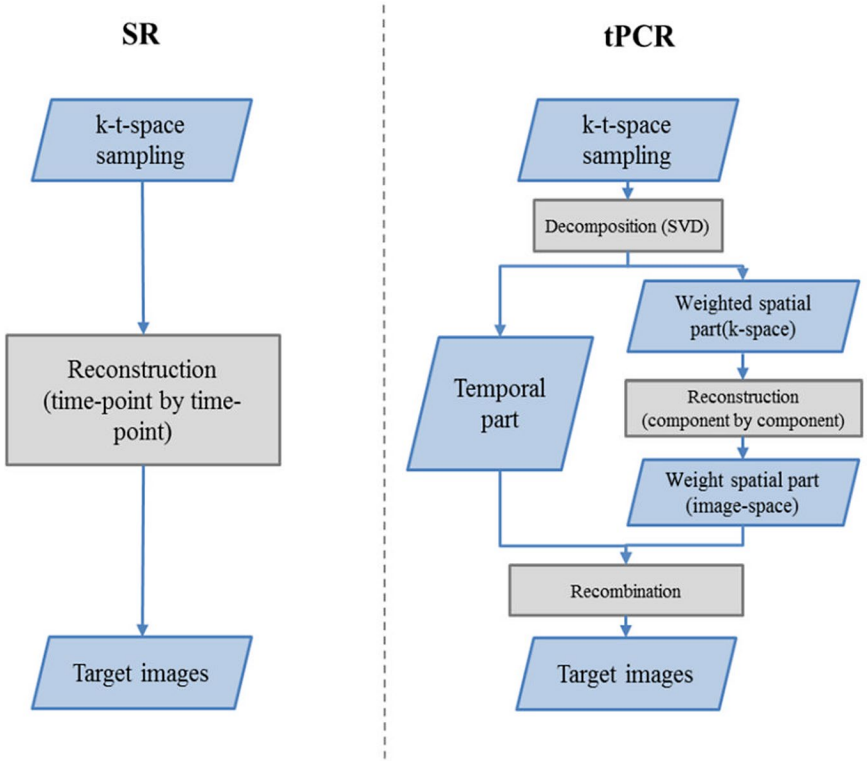

FIGURE 1 Flowchart of conventional time-point-by-time-point sequential reconstruction (SR) and time-domain principal component reconstruction (tPCR) framework

where κ is the condition number of the forward operator. Therefore, the number of iterations n_l to reconstruct the lth principal component is determined by the following equation:

$$n_l = \frac{1}{2}\sqrt{\kappa}\ln\left(\frac{2}{tol \times \frac{\varepsilon_1}{\varepsilon_l}}\right) = n_1 - \frac{1}{2}\sqrt{\kappa}\ln\frac{\varepsilon_1}{\varepsilon_l}, \quad (8)$$

where n_1 is the number of iterations used to reconstruct the first principal component. The condition number κ is not known a priori but can be estimated from the achieved tolerance at each iteration in Equation (7). Although the number of images to reconstruct (either full images or PCA spatial basis images) is the same in SR and tPCR, the different distribution of the number of reconstruction iterations in tPCR may allow for a better or faster reconstruction overall.

3 | METHODS

3.1 | Scanning parameters

MRI data were acquired on a 3T MR scanner (Magnetom Prisma, Siemens, Erlangen, Germany) with a 64-channel head coil. The single-shot 3D MREG sequence with a variable-density stack-of-spirals (SOS) trajectory (TR/TE 100/36 ms, spatial resolution/FOV 3 × 3 × 3/192 × 192 × 150 mm, flip angle 25°) was used.[23] The readout duration is 76 ms with 5 μs dwell time. Dual-phase gradient-echo sequence with different TEs (TE_1 4.92 ms, TE_2 7.38 ms) was acquired to calculate coil sensitivity maps and B_0 field maps. Single-shot single-slice EPI images (TR/TE 100/35 ms, spatial resolution/FOV 3 × 3 × 3/192 × 192 × 3 mm, flip angle 25°) were also acquired to be used as the ground truth in simulation experiments that will be described later. A T1-weighted structural image with 1 × 1 × 3 mm resolution was collected as reference.

The SOS k-space trajectory can be described by four parameters[23]: the radial undersampling rate in the x-y plane, which varies linearly from the center (R1) to the edges (R2) of k-space, and the undersampling rate in the z-direction (spacing between the spirals), which also varies linearly from the center (R3) to the edges (R4) of k-space. The total undersampling rate thus varies from R1 × R3 at the k-space center to R2 × R4 at the periphery. The 3D SOS trajectory used [R1, R2, R3, R4] = [3, 6, 1.6, 3.9], which corresponds to an average undersampling rate (when integrated over k-space) of 12.3.[23]

3.2 | Breath-hold data acquisition and statistical analysis

A breath-hold experiment was performed due to its broad activation including regions with strong off-resonance effects. Three volunteers performed the experiment. The volunteers

gave informed consent and the experimental protocol was approved by the ethics committee of the University Medical Center Freiburg. This experiment was designed as a paced breath-hold paradigm[46] (duration 4 blocks × 37 s = 148 s). Each block began with two 6 s paced breath periods (3 s breath in and 3 s breath out), which is to ensure the subject was just in the state of expiration when starting the breath hold. Then a 15 s hold period and a 10 s free breathing period followed. The same protocol was used for both the 2D single-slice EPI sequence and the 3D MREG sequence.

Data from the first 12 s of the fMRI time-series were discarded in order to reach signal equilibrium. The reconstructed images were preprocessed (realigned and smoothed with 8 mm FWHM) with SPM12 (http://www.fil.ion.ucl.ac.uk/spm), and then analyzed by FMRISTAT (http://www.math.mcgill.ca/keith/fmristat/). The regressor is constructed according to the method in.[47] The SPM canonical HRF and an additional temporal derivative regressor were included in the model, leading to F-statistic maps indicating areas for which the combination of both regressors accounted for a significant amount of signal variance. A 10^{th} order auto-regressive noise model (AR 10) was used to correct for autocorrelations.[48]

3.3 | Simulation study

Simulation experiments were performed with single-slice EPI images and 2D variable-density spirals, which were defined using only parameters R1 and R2. The simulated k-t-space datasets were generated by transforming the ground truth images (1360 normalized single-slice EPI images) with the forward operator based on a 2D spiral trajectory ([R1, R2] = [4, 8]) as well as sensitivity maps and B_0 field map calculated from the dual-phase gradient-echo images. To reduce the computational cost of the various simulations, only the 10 coil sensitivity maps from the coil elements closest to the single slice were included in the forward operator. To ensure that the simulated off-resonance effects were as severe as in real 3D MREG data (see below), the 2D read-out duration was fixed to 76 ms for the various trajectories by lengthening the trajectory dwell time. The reconstruction was the same as 3D MREG except with a different regularization parameter (L2-norm: 0.01, L1-norm: 6×10^{-5}). We shared the source Matlab code and example datasets in https://github.com/feiwang1206/tPCR (commit ccdc4bd314256805423906f7d1bdc81489e60840).

Multiple simulation experiments were performed to make a broad comparison across different conditions:

1. Five different background intensities, which were generated by scaling the original mean temporal image by a factor of 1, 0.8, 0.6, 0.4, 0.2, while keeping the temporal fluctuations identical (except for an offset due to the different background intensities).
2. Three different regularization parameters for L2-norm (0.001, 0.01, 0.1) and L1-norm (6×10^{-6}, 6×10^{-5}, 6×10^{-4}).
3. Three undersampling rates [R1, R2] = [2, 4], [4, 8], [6, 12].
4. Three off-resonance effects intensity with scaling the measured field map by a factor of 0, 1, and 2.

3.4 | 3D MREG reconstruction settings

The MREG reconstruction settings for SR and tPCR were identical. The L2-norm linear CG reconstruction and L1-norm non-linear CG reconstruction with total variation penalty (TV) were applied as described in Hugger et al.[49] The regularization parameters were determined empirically for 3D MREG (L2-norm: 0.05, L1-norm: 5×10^{-6}). Note that for tPCR with L1-norm regularization, the regularization parameter of each component was scaled according to Equation (4) by using the temporal averaged k-space as reference. To correct for off-resonance effects, a time-segmented method was applied in the forward operator.[29] The number of segments was set to 10. The computations were performed on an Intel(R) Xeon(R) CPU X7560 @ 2.27GHz, with usage restricted to a single CPU core.

The only difference between the two reconstructions was the number of iterations. For SR, the reconstructions of all time points were the same: a maximum number of iterations equal to 100, with an additional tolerance 5×10^{-4}. For tPCR, the progressively smaller numbers of iterations for each component were calculated according to Equation (8). Here, n_1 was set so that the total combined number of iterations used to reconstruct all components became equal to that of the SR method. Additionally, to investigate the effects of accelerating the reconstruction, reconstructions were also evaluated when reducing n_1 so that the average number of iterations per component was reduced in steps of 10 with a minimum 5.

4 | RESULTS

4.1 | Simulation study

4.1.1 | The distribution of the number of iterations

Figure 2 presents the distribution of the number of iterations for each reconstruction method. With SR, the required number of iterations is almost identical across all time points. With tPCR, the number of iterations decreases with the logarithm of the component weights, in accordance with

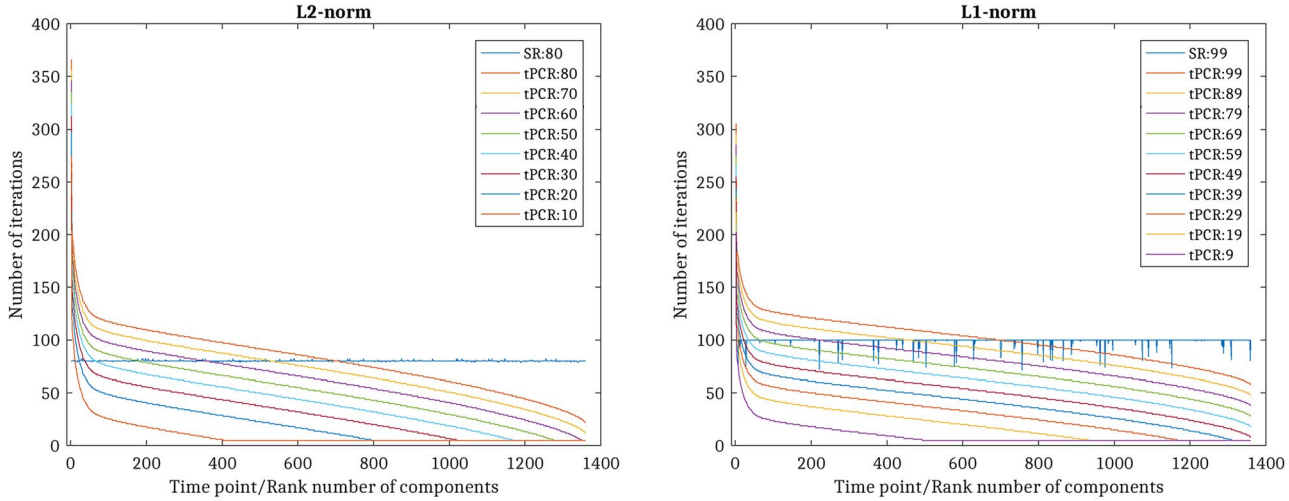

FIGURE 2 Distribution of the number of iterations in sequential reconstruction (SR) and time-domain principal component reconstruction (tPCR) for L2-norm (left) and L1-norm (right) regularizations. The numbers in the legends represent the mean number of iterations per time point (for SR) or per component (for tPCR)

Equation (8). Distributions of the number of iterations are also plotted for reduced values of n_1 so that the mean number of iterations was decreased in steps of 10 (and hence reducing the computational load), leading to an overall shift of the curve. As described previously, the minimum number of iterations was set to 5. Three representative time points from SR and three representative components from tPCR (both the temporal part and the weighted spatial part) with equal mean number of iterations are presented in supporting information Figure S1.

4.1.2 | Reconstruction error

Three types of error were considered in order to evaluate the performance of SR and tPCR: the total error, dynamic error, and activation error. The total error and dynamic error are the absolute value of the difference between the reconstructed images and the ground truth before and after removing the temporal average from the time-series, respectively. The activation errors were defined as differences in the F-statistic maps from ground truth data compared to the maps from reconstructed data. The error percentage was relative to the total signal. To compare with activation error, the total error and dynamic error were calculated on the preprocessed data.

Figure 3 shows the three types of errors as a function of the mean number of iterations across three subjects. Overall, the reconstruction errors in tPCR decrease or keep almost constant as the number of iterations increases, and they are always lower than in SR when using the same mean number of iterations, that is, the same computational load. Alternatively, tPCR achieves the same dynamic error as SR using about 4 times less computational power in L2-norm reconstructions. In L1-norm reconstructions, the errors of tPCR are always lower than SR even when using the minimum number of iterations.

When using the same mean number of iterations during the reconstruction, it is seen that errors are largest in frontal brain regions, which are the ones most affected by off-resonance effects (as shown in Figure 4A, using subject 1 as a representative example). The time-series in these regions (Figure 4B) illustrates the signal deviations from the ground truth, which are larger in SR than tPCR, especially when using L1-norm regularization. With tPCR, the deviations increase when using a lower number of iterations. In contrast, the time-series in regions far away from off-resonance effects (Figure 4C) are reconstructed accurately by both methods.

We also present the difference between SR and tPCR (tPCR - SR) on the SD of the time-series at each voxel as well as the F-statistic maps of subject 1 in Figure 5. Overall, the activation maps show similar behavior as the SD maps. The largest differences are seen in the frontal brain areas. With L2-norm regularization, SR results in lower time-series SDs, consistent with the suppression of BOLD fluctuations, and thus weaker activations than tPCR. With L1-norm regularization, SR results in higher time-series SDs, consistent with the appearance of spurious fluctuations.

4.1.3 | Comparison under different experimental conditions

1. Background intensity

Figure 6 shows the relationship between error and background intensity. For comparison, the error percentage is all relative to the total signal with scaling factor 1 and the

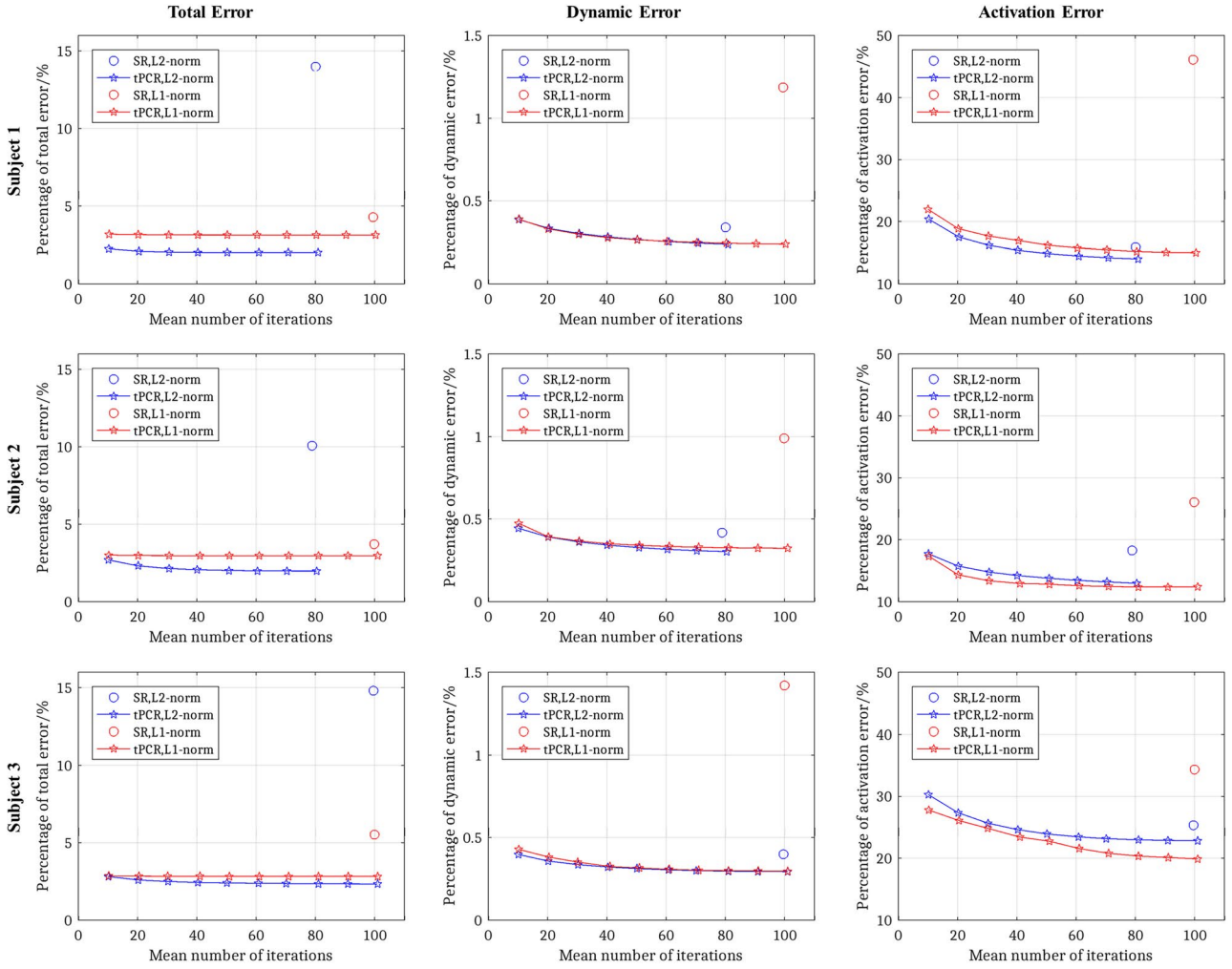

FIGURE 3 Percentage of total error, dynamic error, and activation error of sequential reconstruction (SR) and time-domain principal component reconstruction (tPCR) (the latter as a function of the mean number of iterations) with respect to the ground truth in three subjects. With SR, the total errors are lower with L1-norm regularization, but the dynamic errors and activation errors are lower with L2-norm regularization. With tPCR, all types of errors are lower for both L1-norm and L2-norm regularization

number of iterations is also identical with scaling factor 1. The total error, no matter the reconstruction method and regularization type, is almost proportional to background intensity. However, the dynamic error remains constant except for SR with L1-norm, where it is approximately proportional to background intensity.

2. Regularization parameters

The errors under various regularization parameters are presented in Figure 7 as a function of the number of iterations. With L2-norm, the total errors and dynamic errors were always lower with tPCR than with SR when using the same mean number of iterations, but the difference became very small when using a larger number of iterations. With L1-norm, the total errors of tPCR are also lower than SR except when using a larger number of iterations, but the dynamic errors with SR still did not converge to the lower values obtained with tPCR, even with a large number of iterations. Overall, the convergence speed is faster at large regularization parameters than at smaller regularization parameters.

3. Undersampling rate and off-resonance effects intensity

The errors under various undersampling rates and off-resonance effects intensity are presented in Figure 8. Overall, the total errors and dynamic errors increase with undersampling rate and off-resonance effects intensity. Differences in the errors between both reconstruction methods, as well as differences in the rate of increase of errors as a function of undersampling rate and field scaling factor, were investigated by 2-way repeated-measures analysis of variance on the effects of reconstruction method and undersampling rate/field scaling factor. For total errors, the errors increased in all cases significantly faster in SR than in tPCR. For dynamic

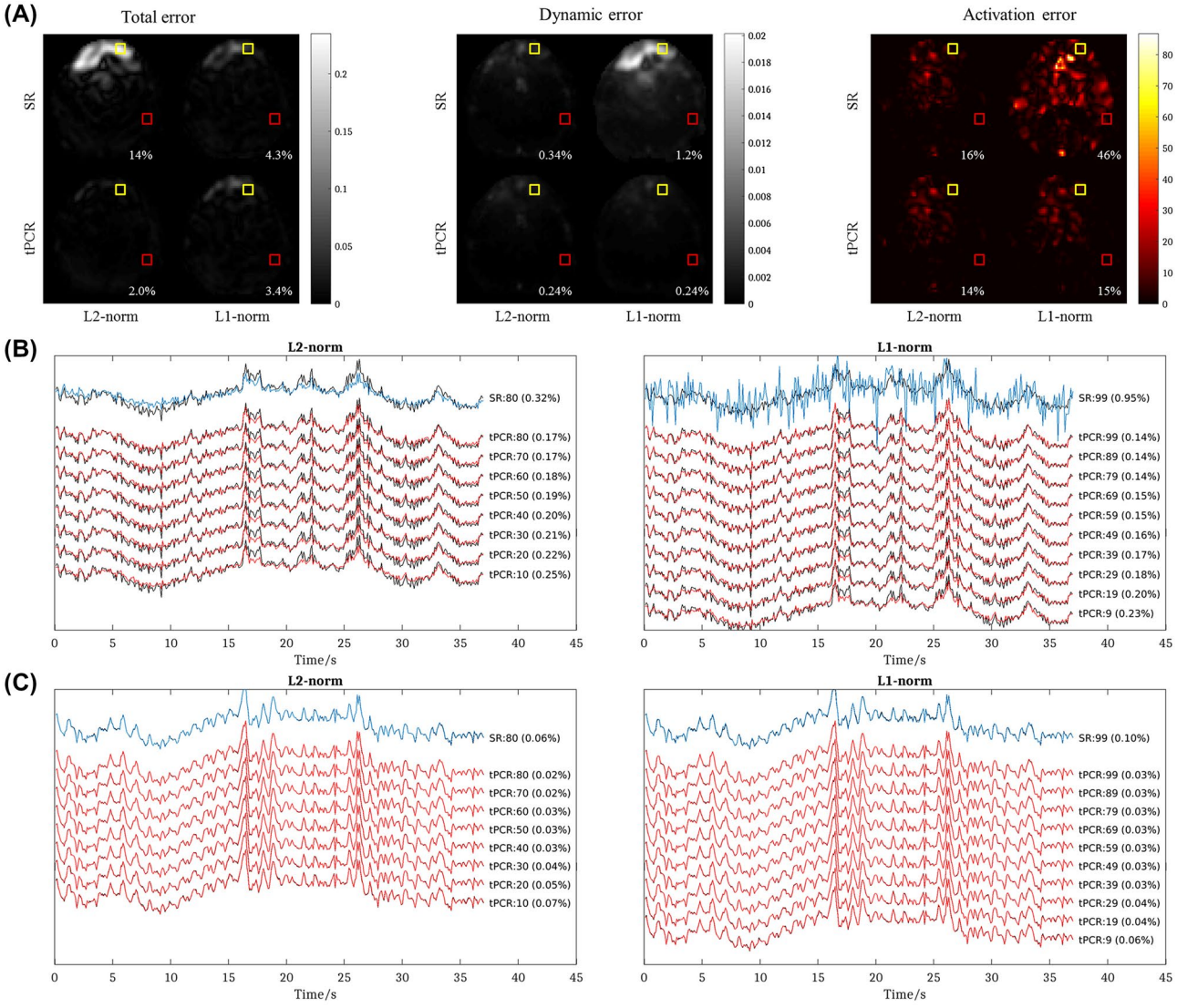

FIGURE 4 (A) Spatial distribution of the three types of error in subject 1 when using the same mean number of iterations for sequential reconstruction (SR) and time-domain principal component reconstruction (tPCR) (80 for L2-norm, 99 for L1-norm), with the error percentage shown in the corner of each image. Similar to Figure 3, SR results in larger total errors with L2-norm regularization and larger dynamic errors and activation errors with L1-norm regularization. The errors are most prominent in frontal brain regions. All three types of errors are lower with tPCR. (B) De-meaned time-series (first 37 s) of the voxel in the yellow box in (A) with SR (blue) and tPCR with various numbers of iterations (red). The ground truth time-series is plotted in black. (C) De-meaned time-series (first 37 s) of the voxel in the red box in (A). Here, the ground truth time-series is not visible because it is undistinguishable from the reconstructed time-series

errors, the rate of increase was also significantly higher in SR than in tPCR when using L1-norm regularization but not when using L2-norm regularization. The *P* value in each subgroup in each figure shows the statistical difference between SR and tPCR at each level of undersampling rate or field scaling factor. For L2-norm, both total errors and dynamic errors were significantly lower in tPCR than in SR in all cases. For L1-norm, total errors were significantly different only at the largest undersampling rate, but the dynamic errors showed obvious differences. Only for the largest field scaling factor was the difference marginally nonsignificant ($P = .063$), although this could be attributed to the low number of subjects and the large variability in the error values in SR.

4.2 | 3D MREG study

For experiments using real data, in the absence of ground truth, we only compare the difference of SD maps and the F-statistic maps of three subjects between SR and tPCR (tPCR-SR) in Figure 9. Overall, the activation maps show similar behavior as the SD maps and the largest differences are seen around the nasal cavity. With L2-norm regularization, SR results in lower time-series SDs and weaker activations. With L1-norm regularization, the higher instability of the nonlinear reconstruction results in more widespread differences, but the largest differences are seen in frontal brain areas. All reconstructed slices for all reconstruction

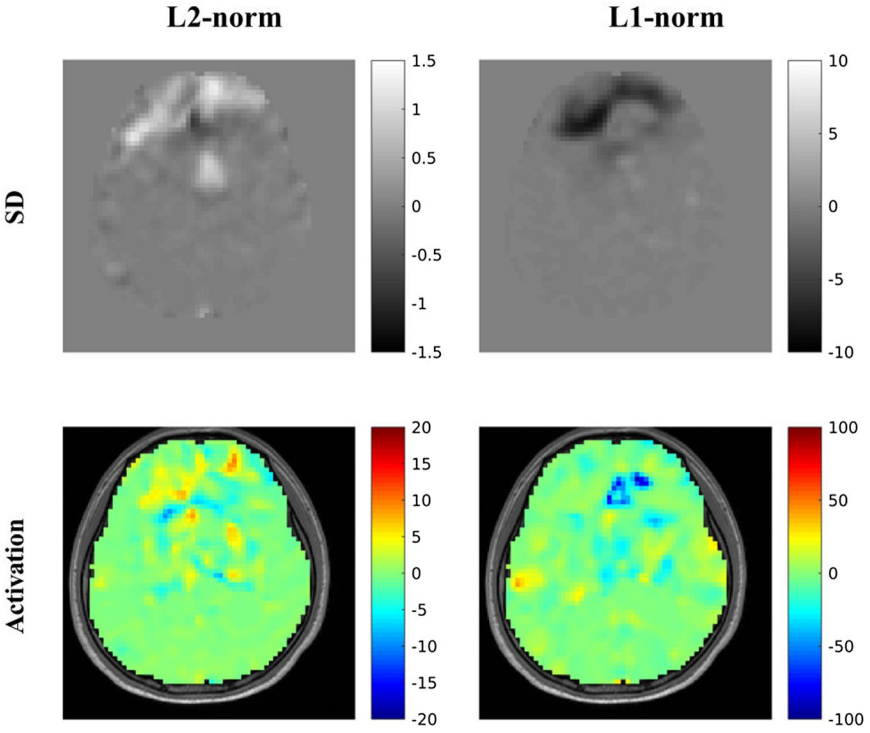

FIGURE 5 The difference of SD maps (the first row) and F-statistic activation maps (the second row) of subject 1 between sequential reconstruction (SR) and time-domain principal component reconstruction (tPCR) when using the same mean number of iterations for them (80 for L2-norm, 99 for L1-norm)

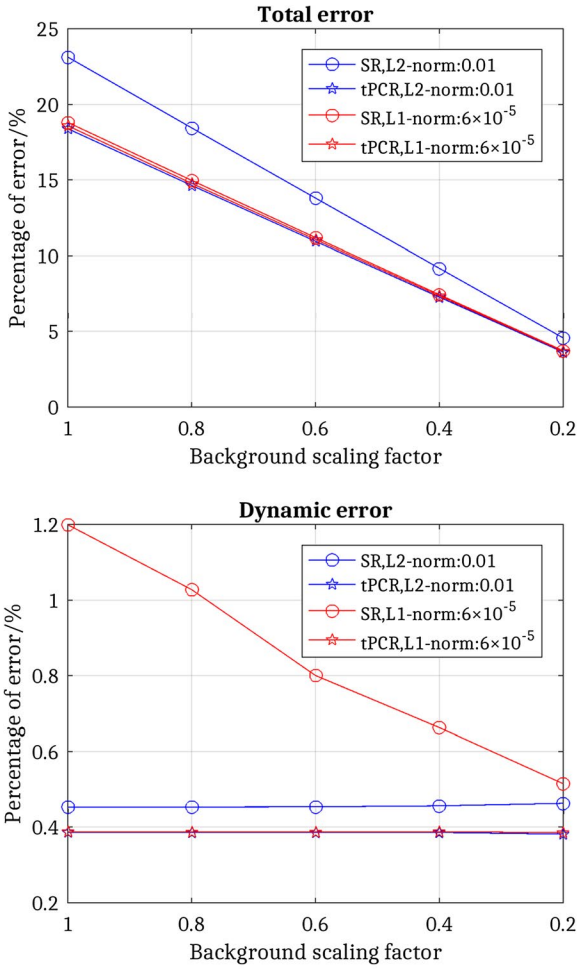

FIGURE 6 Plots of total errors and dynamic errors as a function of background intensity

types are shown in supporting information Figure S2. All the SD maps and activation maps for three subjects and two examples of time-series from region with and without strong off-resonance effects are shown in supporting information Figure S3.

The computational costs of SR and tPCR (under various mean numbers of iterations) are listed in Table 1. The time spent on decomposition and combination (steps 1 and 3) is negligible relative to the reconstruction itself (step 2). When using a low mean number of iterations, tPCR is about 6 times faster than SR.

5 | DISCUSSION

The presented tPCR reconstruction framework provides a new methodology for iterative CG-SENSE reconstruction of fMRI data. Normally, images at each time point are reconstructed independently. However, the proposed tPCR method performs the reconstruction in the decomposed principal component space with redistributed computational cost according to the weight of each component. It is shown that tPCR yields fewer temporal dynamic errors, and thus fewer activation errors, than SR across different regularization parameters, undersampling rates, and off-resonance effects intensities with the same computational costs, especially when using L1-norm nonlinear reconstruction. In turn, for a given error level, tPCR also offers the opportunity to considerably reduce the computational costs compared to SR. Although the current work was applied to the CG-SENSE reconstruction of MREG data, it

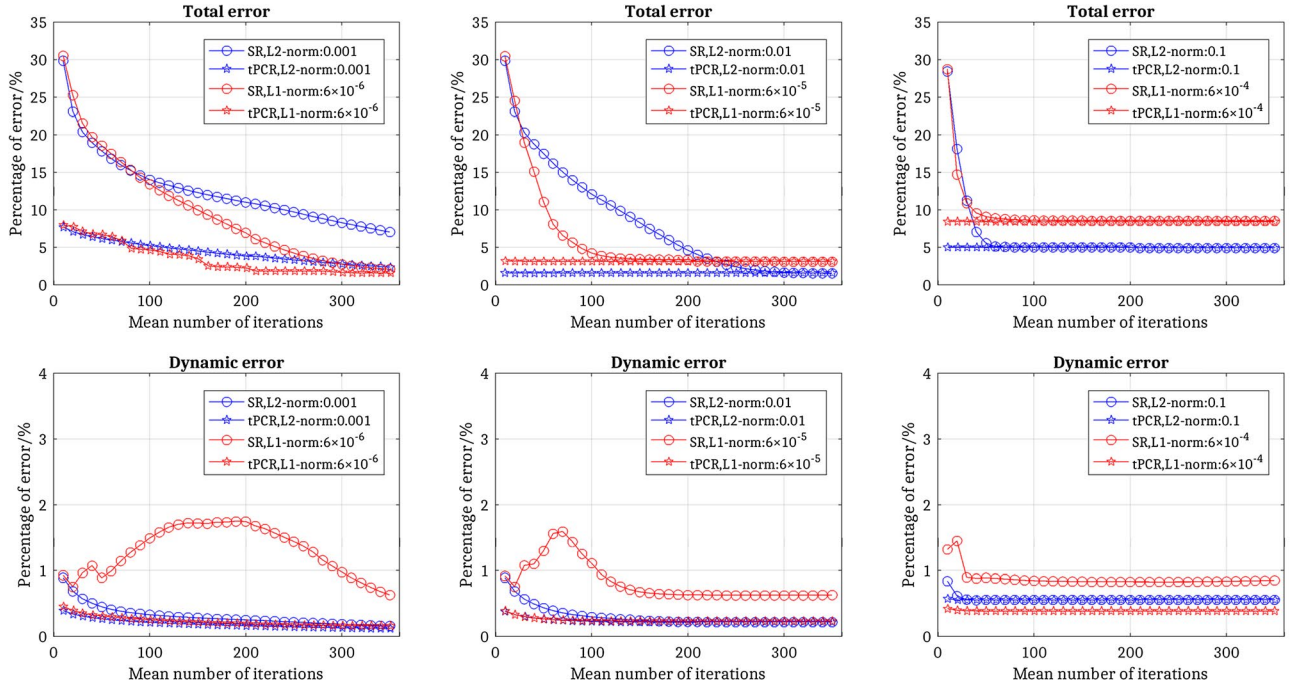

FIGURE 7 Plots of total errors and dynamic errors as a function of the mean number of iterations for sequential reconstruction (SR) and time-domain principal component reconstruction (tPCR) when using various regularization parameters (with each column corresponding to different values, as shown in the legend) for L1-norm and L2-norm reconstructions

would be applicable to any other iterative reconstruction of dynamic MR data.

5.1 | Reconstruction efficiency

One benefit of tPCR is the improved reconstruction efficiency relative to SR, which works for both L2-norm and L1-norm reconstructions. The reconstruction efficiency refers to the average rate of convergence of the iterative algorithm over the whole fMRI datasets. In highly ill-conditioned cases, such as MREG here, reconstruction of an entire dataset may require hundreds of CPU-hours (see Table 1).

With the conventional SR framework, the rate of convergence is essentially the same for each image, as fMRI images are highly similar to each other. However, in tPCR, high-rank components can be reconstructed much faster, because they contribute less to the total signal than low-rank components. Even though the number of principal components is equal to the number of time points, overall the mean number of iterations of tPCR is less than SR while attaining a similar level of dynamic error, as demonstrated in Figure 3. Additional computational overhead for the decomposition and combination steps is required in tPCR, but this is negligible relative to the reconstruction itself, so the total computational cost is significantly reduced. Instead of reducing computational costs, it would also be possible to increase the average number of iterations in tPCR up to the same computational load as in SR; this leads to less reconstruction error in tPCR than in SR, yielding a more accurate fMRI analysis. Note that with a sufficient number of iterations, both reconstruction methods converge to the same solution $\left(\mathbf{F}^{\mathrm{T}}\mathbf{F}+\lambda^2\mathbf{R}\right)^{-1}\mathbf{F}^{\mathrm{T}}\boldsymbol{s}$ when using L2-norm regularization, as shown in Figure 7; however, tPCR converges faster. It thus appears that the source of reconstruction errors in SR is an insufficient number of iterations to reach full convergence. The number of iterations had been chosen according to a previous study[49]; however, that work investigated fMRI activations in visual and motor cortices, where susceptibility artifacts do not play a major role. However, in areas such as the frontal lobe, off-resonance effects lead to a loss of conditioning (see section 5.3) and thus would require a much larger number of iterations to reach convergence. Even though off-resonance effects are essentially a static image feature, the lack of convergence will lead to reconstruction errors that will show up as spurious time-series fluctuations. This is less of an issue in tPCR, which converges in a low average number of iterations anyway.

5.2 | Reconstruction stability

Even stronger differences between tPCR and SR were observed when using L1-norm nonlinear reconstruction. L1-norm was proposed for its tendency to prefer sparse

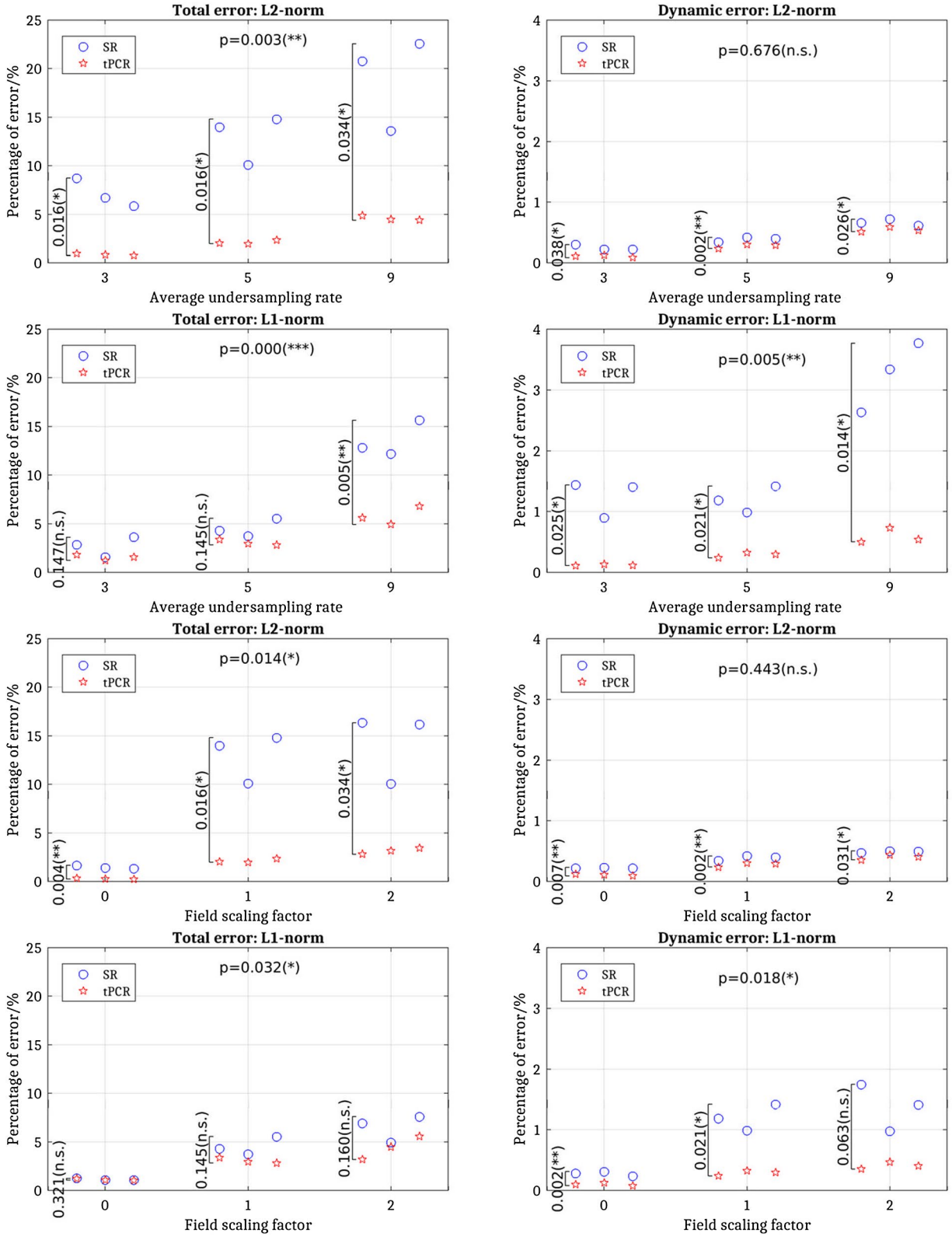

FIGURE 8 Relationship of total errors and dynamic errors with average undersampling rate/field scaling factor for sequential reconstruction (SR) and time-domain principal component reconstruction (tPCR) using L1-norm and L2-norm regularization. Each group includes the value of three subjects. The *P* value on top of each figure refers to the effect of the undersampling rate/field scaling factor on the rate of error increase, whereas the *P* value within each group corresponds to the statistical difference between SR and tPCR at each level of the undersampling rate and field scaling factor. Behind the *P* value, ***, **, * and n.s. correspond to $P < .001$, $P < .01$, $P < .05$, and $P \geq .05$ respectively

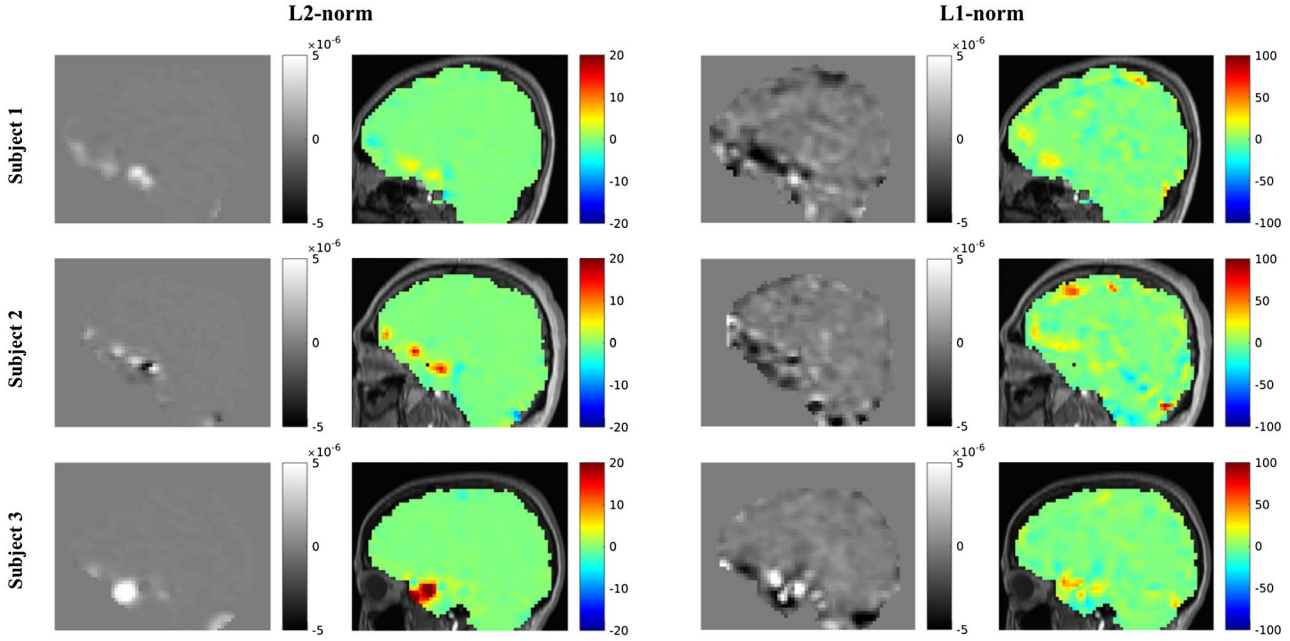

FIGURE 9 Results of 3D magnetic resonance encephalography (MREG) breath-hold experiments in one sagittal slice of three subjects. (A) the difference of SD maps and activation maps between sequential reconstruction (SR) and time-domain principal component reconstruction (tPCR) when using the same mean number of iterations for them (68 for L2-norm, 60 for L1-norm)

TABLE 1 The computational costs of SR and tPCR under various mean numbers of iterations (all times are in CPU-hours). Steps 1-3 in tPCR refer to decomposition, reconstruction of principal components, and recombination, respectively

	SR	tPCR (step 1)	tPCR (step 2)							tPCR (step 3)
L2-norm										
Sub 1	63 (428 h)*	2h	64 (435 h)	54 (367 h)	44 (299 h)	34 (231 h)	24 (163 h)	14 (95 h)		0.3 h
Sub 2	67 (456 h)	2 h	68 (562 h)	58(394 h)	48 (326 h)	38 (258 h)	28 (190 h)	18 (122 h)	8 (54 h)	0.3 h
Sub 3	67 (456 h)	2 h	69 (469 h)	59 (401 h)	49 (333 h)	39 (265 h)	29 (197 h)	19 (129 h)	9 (61 h)	0.3 h
L1-norm										
Sub 1	58 (526 h)	2 h	58 (526 h)	48 (435 h)	38 (345 h)	28 (254 h)	18 (163 h)	8(73 h)		0.3 h
Sub 2	60(544 h)	2 h	60 (544 h)	50 (453 h)	40 (363 h)	30 (272 h)	20(181 h)	10 (91 h)		0.3 h
Sub 3	57 (517 h)	2 h	59 (535 h)	49 (444 h)	39 (354 h)	29 (263 h)	19 (172 h)	9 (82 h)		0.3 h

Abbreviations: CPU, central processing unit; SR, sequential reconstruction; tPCR, time-domain principal component reconstruction.

*63 is the mean number of iterations, 428 CPU-hours is the corresponding computational cost for 1360 time points.

solutions.[22] This is also demonstrated by the smaller total errors in L1-norm regularization than L2-norm regularization, as shown in Figures 3 and 4, and this had also been previously reported for MREG reconstruction.[49] However, this is no longer true when looking at the dynamic errors, which are more relevant for fMRI analyses.

The nonlinear CG algorithm used in L1-norm reconstruction could introduce increasing variance due to a larger number of iterations and potentially several restarts. This may lead to inherent instability when using a large number of iterations in ill-conditioned cases, leading to diverging solutions.[50] This reconstruction instability may lead to increasing dynamic error. Moreover, unlike linear reconstructions, the reconstruction operator is data dependent (see section 2.1) and will thus yield different solutions for the different decompositions used in SR and tPCR. Indeed, simulation experiments (Figure 6) demonstrated that the dynamic error in SR is approximately proportional to the magnitude of background signal, even though this signal is merely an offset of the fMRI temporal variation signal, which was fixed. In fMRI, the background is usually much stronger than the dynamic part; thus the dynamic error is much higher with SR. With tPCR, the background has far less influence on the dynamic error, because the background (mainly in the first component) is reconstructed separately from the dynamic part (mainly

in high-rank components). Therefore, dynamic errors are smaller in tPCR than in SR, even when using a large number of iterations (Figure 7).

It should also be noted that the regularization parameters were simply scaled according to the magnitude of the spatial basis functions (Equation (4)) and were thus not specifically optimized for tPCR. It is possible, for example, that these spatial components have different sparsities than full images and would thus benefit from nonlinear L1-norm reconstruction. Future studies will investigate the possibility to optimize the regularization of the spatial basis components, which could have the potential to improve the performance of tPCR even further.

5.3 | Robustness to regularization, undersampling, and off-resonance effects

One common consequence of regularization, undersampling, and/or off-resonance effects is that they all have an effect on ill-conditioning and convergence speed of iterative algorithms. A high regularization parameter improves the conditioning, whereas undersampling directly increases the degree of ill-conditioning. According to the theory of local k-space,[51] an external inhomogeneous magnetic field reduces the conditioning by locally distorting the k-space trajectory. In Figures 7 and 8, tPCR shows faster convergence speed across regularization parameters and only modest increases in dynamic errors with undersampling and off-resonance effects than SR. Thus, tPCR is more robust to regularization, undersampling, and off-resonance effects.

Importantly, the simulation results could be replicated in real MREG data. Despite the lack of ground truth, differences in the SD of the time-series, and the resulting effects on activation maps, were largely consistent with the results of the simulation experiments (Figures 5 and 9).

5.4 | Other decomposition methods

Besides PCA in tPCR, other decomposition methods could also be used, such as simple background separation or Fourier decomposition. As long as the decomposition can separate the background from the dynamic components, it can reduce the dynamic error when using L1-norm regularization. But tPCR could provide the highest reconstruction efficiency because it is the densest expression of data, and some of the principal components may become sparser and thus contribute less error.

5.5 | Other applications

It should be noticed that the tPCR method is not itself a reconstruction algorithm but is rather a framework to improve the overall efficiency and stability of a given dynamic imaging reconstruction algorithm. Consequently, this method has the potential to be used in other classes of iterative reconstructions than CG-SENSE. This may include, for example, GRAPPA-based iterative reconstruction, typically SPIRiT and ESPIRiT in which an iterative algorithm is used to find the optimal k-space or image at each time point independently.[52,53] Another example is typical GRAPPA or simultaneous multislice (SMS) imaging if performed with integrated sampling (i.e., sampling the auto-calibration lines within each time point), in which the kernel functions are iteratively estimated at each time point. Here, tPCR could allow a more accurate estimation of the dynamic kernels. Finally, tPCR could also be applied to nonlinear reconstructions that try to recover dynamic sensitivity maps, T2* maps, or field maps jointly with the images themselves.[28,54]

6 | CONCLUSIONS

This proof-of-concept study compared standard time-point-by-time-point SR framework and a PCA-based tPCR framework for the iterative reconstruction of fast fMRI data. The tPCR outperforms the SR on two aspects: (1) improving reconstruction efficiency and (2) improving reconstruction stability of nonlinear reconstructions. These two improvements are robust to regularization, undersampling, and off-resonance effects and in turn give a chance to significantly reduce the computation cost and/or improve reconstruction quality.

ACKNOWLEDGMENTS

This work was supported by the DFG Koselleck grant He 1875/28-1, the cluster of excellence EXC-1086 BrainLinks-BrainTools from the DFG, and the China Scholarship Council (CSC).

ORCID

Fei Wang https://orcid.org/0000-0002-2675-2791

TWITTER

Fei Wang @FeiWang67466739

REFERENCES

1. Ogawa S, Lee T-M, Kay AR, Tank DW. Brain magnetic resonance imaging with contrast dependent on blood oxygenation. *Proceedings of the National Academy of Sciences*. 1990;87:9868–9872.
2. Glover GH. Overview of functional magnetic resonance imaging. *Neurosurg Clin N Am*. 2011;22:133–139.
3. Lewis LD, Setsompop K, Rosen BR, Polimeni JR. Fast fMRI can detect oscillatory neural activity in humans. *Proceedings of the National Academy of Sciences*. 2016;113:E6679–E6685.
4. Lee H-L, Zahneisen B, Hugger T, LeVan P, Hennig J. Tracking dynamic resting-state networks at higher frequencies using MR-encephalography. *NeuroImage*. 2013;65:216–222.

5. Handwerker DA, Ollinger JM, D'Esposito M. Variation of BOLD hemodynamic responses across subjects and brain regions and their effects on statistical analyses. *NeuroImage*. 2004;21:1639–1651.
6. Dilharreguy B, Jones RA, Moonen CTW. Influence of fMRI data sampling on the temporal characterization of the hemodynamic response. *NeuroImage*. 2003;19:1820–1828.
7. Proulx S, Safi-Harb M, LeVan P, An D, Watanabe S, Gotman J. Increased sensitivity of fast BOLD fMRI with a subject-specific hemodynamic response function and application to epilepsy. *NeuroImage*. 2014;93:59–73.
8. Hennig J, Zhong K, Speck O. MR-Encephalography: fast multi-channel monitoring of brain physiology with magnetic resonance. *NeuroImage*. 2007;34:212–219.
9. Krüger G, Glover GH. Physiological noise in oxygenation-sensitive magnetic resonance imaging. *Magn Reson Imaging*. 2001;46:631–637.
10. Boyacioğlu R, Barth M. Generalized inverse imaging (GIN): Ultrafast fMRI with physiological noise correction. *Magn Reson Med*. 2013;70:962–971.
11. Lin F-H, Nummenmaa A, Witzel T, et al. Physiological noise reduction using volumetric functional magnetic resonance inverse imaging. *Hum Brain Mapp*. 2012;33:2815–2830.
12. Kiviniemi V, Wang X, Korhonen V, et al. Ultra-fast magnetic resonance encephalography of physiological brain activity-Glymphatic pulsation mechanisms? *J Cereb Blood Flow Metab*. 2016;36:1033–1045.
13. Feinberg DA, Moeller S, Smith SM, et al. Multiplexed echo planar imaging for sub-second whole brain FMRI and fast diffusion imaging. *PLoS ONE*. 2010;5:e15710.
14. Posse S, Ackley E, Mutihac R, et al. Enhancement of temporal resolution and BOLD sensitivity in real-time fMRI using multi-slab echo-volumar imaging. *NeuroImage*. 2012;61:115–130.
15. Jacobs J, Stich J, Zahneisen B, et al. Fast fMRI provides high statistical power in the analysis of epileptic networks. *NeuroImage*. 2014;88:282–294.
16. Akin B, Lee H-L, Hennig J, LeVan P. Enhanced subject-specific resting-state network detection and extraction with fast fMRI. *Hum Brain Mapp*. 2017;38:817–830.
17. Smith SM, Beckmann CF, Andersson J, et al. Resting-state fMRI in the human connectome project. *NeuroImage*. 2013;80:144–168.
18. LeVan P, Akin B, Hennig J. Fast imaging for mapping dynamic networks. *NeuroImage*. 2018;180:547–558.
19. Pruessmann KP, Weiger M, Scheidegger MB, Boesiger P. SENSE: sensitivity encoding for fast MRI. *Magn Reson Med*. 1999;42:952–962.
20. Pruessmann KP. Encoding and reconstruction in parallel MRI. *NMR Biomed*. 2006;19:288–299.
21. Griswold MA, Jakob PM, Heidemann RM, et al. Generalized autocalibrating partially parallel acquisitions (GRAPPA). *Magn Reson Med*. 2002;47:1202–1210.
22. Gamper U, Boesiger P, Kozerke S. Compressed sensing in dynamic MRI. *Magn Reson Med*. 2008;59:365–373.
23. Assländer J, Zahneisen B, Hugger T, et al. Single shot whole brain imaging using spherical stack of spirals trajectories. *NeuroImage*. 2013;73:59–70.
24. Zahneisen B, Grotz T, Lee KJ, et al. Three-dimensional MR-encephalography: fast volumetric brain imaging using rosette trajectories. *Magn Reson Med*. 2011;65:1260–1268.
25. Zahneisen B, Hugger T, Lee KJ, et al. Single shot concentric shells trajectories for ultra fast fMRI. *Magn Reson Med*. 2012;68:484–494.
26. Pruessmann KP, Weiger M, Börnert P, Boesiger P. Advances in sensitivity encoding with arbitrary k-space trajectories. *Magn Reson Med*. 2001;46:638–651.
27. Davids M, Ruttorf M, Zöllner FG, Schad LR. Fast and robust design of time-optimal k-space trajectories in MRI. *IEEE Trans Med Imaging*. 2015;34:564–577.
28. Sutton BP. *Physics Based Iterative Reconstruction for MRI: Compensating and Estimating Field Inhomogeneity and T2 Relaxation*. Ann Arbor, Michigan: The University of Michigan; 2003.
29. Sutton BP, Noll DC, Fessler JA. Fast, iterative image reconstruction for MRI in the presence of field inhomogeneities. *IEEE Trans Med Imaging*. 2003;22:178–188.
30. Kadah YM, Xiaoping HU. Simulated phase evolution rewinding (SPHERE): a technique for reducing B0 inhomogeneity effects in MR images. *Magn Reson Med*. 1997;38:615–627.
31. Fischer A, Breuer F, Blaimer M, Seiberlich N, Jakob PM. Accelerated dynamic imaging by reconstructing sparse differences using compressed sensing. In Proceedings of the 16th Annual Meeting of ISMRM, Toronto, Canada, 2008. p. 3–9.
32. Cao Z, Sukhoon OH, Otazo R, Sica CT, Griswold MA, Collins CM. Complex difference constrained compressed sensing reconstruction for accelerated PRF thermometry with application to MRI-induced RF heating. *Magn Reson Med*. 2015;73:1420–1431.
33. Wang H, Miao Y, Zhou K, et al. Feasibility of high temporal resolution breast DCE-MRI using compressed sensing theory. *Med Phys*. 2010;37:4971–4981.
34. Otazo R, Candès E, Sodickson DK. Low-rank plus sparse matrix decomposition for accelerated dynamic MRI with separation of background and dynamic components. *Magn Reson Med*. 2015;73:1125–1136.
35. Singh V, Tewfik AH, Ress DB. Under-sampled functional MRI using low-rank plus sparse matrix decomposition. In Acoustics, Speech and Signal Processing (ICASSP), 2015 IEEE International Conference on, 2015;897–901.
36. Trémoulhéac B, Dikaios N, Atkinson D, Arridge SR. Dynamic MR image reconstruction-separation from undersampled (k, t)-space via low-rank plus sparse prior. *IEEE Transactions on Medical Imaging*. 2014;33:1689–1701.
37. Liang Z-P. Spatiotemporal imagingwith partially separable functions. In Biomedical Imaging: From Nano to Macro, 2007. ISBI 2007. 4th IEEE International Symposium on, 2007;988–991.
38. Gupta SA, Liang ZP. Dynamic imaging by temporal modeling with principal component analysis. In Proceedings of the 9th Annual Meeting of ISMRM, Adelaide, Australia, 2001. p. 10.
39. Pedersen H, Kozerke S, Ringgaard S, Nehrke K, Kim WY. k-t PCA: temporally constrained k-t BLAST reconstruction using principal component analysis. *Magn Reson Med*. 2009;62:706–716.
40. Haldar JP, Liang Z-P. Spatiotemporal imaging with partially separable functions: A matrix recovery approach. In Biomedical Imaging: From Nano to Macro, 2010 IEEE International Symposium on, 2010;716–719.
41. Lingala SG, Yue HU, DiBella E, Jacob M. Accelerated dynamic MRI exploiting sparsity and low-rank structure: kt SLR. *IEEE Trans Med Imaging*. 2011;30:1042–1054.
42. Chiew M, Smith SM, Koopmans PJ, Graedel NN, Blumensath T, Miller KL. k-t FASTER: acceleration of functional MRI

data acquisition using low rank constraints. *Magn Reson Med*. 2015;74:353–364.
43. Tsao J, Boesiger P, Pruessmann KP. k-t BLAST and k-t SENSE: dynamic MRI with high frame rate exploiting spatiotemporal correlations. *Magn Reson Med*. 2003;50:1031–1042.
44. Wang F, Juergen H, LeVan P. k-t Rank Separation Reconstruction for non-Cartesian parallel fMRI. In Proceedings of the 25th Annual Meeting of ISMRM, Honolulu, HI, 2017. Abstract 1521.
45. Shewchuk JR. *An Introduction to the Conjugate Gradient Method without the Agonizing Pain*. Pittsburgh, Pennsylvania: Carnegie-Mellon University, Department of Computer Science; 1994.
46. Bright MG, Murphy K. Reliable quantification of BOLD fMRI cerebrovascular reactivity despite poor breath-hold performance. *NeuroImage*. 2013;83:559–568.
47. Peacock J, Black D, DeLone D, Welker K. Use of a simple breath-holding task for cerebrovascular reactivity scans in clinical functional MR imaging. *Neurographics*. 2016;6:213–218.
48. Jacobs J, Menzel A, Ramantani G, et al. Negative BOLD in default-mode structures measured with EEG-MREG is larger in temporal than extra-temporal epileptic spikes. *Front Neurosci*. 2014;8:335.
49. Hugger T, Zahneisen B, LeVan P, et al. Fast undersampled functional magnetic resonance imaging using nonlinear regularized parallel image reconstruction. *PLoS ONE*. 2011;6:e28822.
50. Peng QU, Zhong K, Zhang B, Wang J, Shen GX. Convergence behavior of iterative SENSE reconstruction with non-Cartesian trajectories. *Magn Reson Med*. 2005;54:1040–1045.
51. Noll DC. Rapid MR image acquisition in the presence of background gradients. In Biomedical Imaging, 2002. Proceedings. 2002 IEEE International Symposium on, 2002;725–728.
52. Lustig M, Pauly JM. SPIRiT: iterative self-consistent parallel imaging reconstruction from arbitrary k-space. *Magn Reson Med*. 2010;64:457–471.
53. Uecker M, Lai P, Murphy MJ, et al. ESPIRiT—an eigenvalue approach to autocalibrating parallel MRI: where SENSE meets GRAPPA. *Magn Reson Med*. 2014;71:990–1001.
54. Uecker M, Hohage T, Block KT, Frahm J. Image reconstruction by regularized nonlinear inversion—joint estimation of coil sensitivities and image content. *Magn Reson Med*. 2008;60:674–682.

SUPPORTING INFORMATION

Additional Supporting Information may be found online in the Supporting Information section.

FIGURE S1 (A) Three reconstructed images using sequential reconstruction (SR) with L2-norm regularization (left) and L1-norm regularization (right). (B) Three reconstructed spatial components (note the different amplitude scales) with L2-norm regularization (left) and L1-norm regularization (right) and corresponding temporal components (real part, only the first 37 s are shown) using time-domain principal component reconstruction (tPCR). With SR, the images at different time points show similar image magnitudes and relatively low image quality, especially for L2-norm. With tPCR, the components exhibit progressively reduced image magnitudes. Component 1 captures most of the image information with almost constant temporal variation, whereas component 5 only captures some local image power but with strong temporal oscillations, and component 1360 has a small magnitude with noise-like spatial and temporal components. In addition, component 1 exhibits a better image quality than images reconstructed by SR due to the much higher number of iterations (see Figure 2)

FIGURE S2 One example 3D magnetic resonance encephalography (MREG) image reconstructed by different regularization types and reconstruction methods from three subjects

FIGURE S3 (A) The SD maps. (B) The activation maps of three subjects. (C) De-meaned time-series (first 37 s) of the voxel in the yellow box in (A) and (B) with SR (blue) and time-domain principal component reconstruction (tPCR) with various numbers of iterations (red), which is strongly affected by off-resonance effects. It shows that tPCR could lead to less noisy time-series than SR, especially when using L1-norm regularization. Meanwhile, it also appears that high frequency fluctuations present in the tPCR time-series actually decrease with the decrease in mean number of iterations. (D) De-meaned time-series (first 37 s) of the voxel in the black box in (A) and (B), which is not affected by off-resonance effects. There is no obvious difference between SR and tPCR, even when the mean number of iterations of tPCR is very low. The texts behind the curves in (C) and (D) are the corresponding reconstruction method and mean number of iterations

How to cite this article: Wang F, Hennig J, LeVan P. Time-domain principal component reconstruction (tPCR): A more efficient and stable iterative reconstruction framework for non-Cartesian functional MRI. *Magn Reson Med*. 2020;00:1–15. https://doi.org/10.1002/mrm.28208